

Three-dimensional processing maps and microstructural evolution of a CNT-reinforced Al-Cu-Mg nanocomposite



F. Mokdad^a, D.L. Chen^{a,*}, Z.Y. Liu^b, D.R. Ni^b, B.L. Xiao^b, Z.Y. Ma^{b,*}

^a Department of Mechanical and Industrial Engineering, Ryerson University, 350 Victoria Street, Toronto, Ontario, Canada M5B 2K3

^b Shenyang National Laboratory for Materials Science, Institute of Metal Research, Chinese Academy of Sciences, 72 Wenhua Road, Shenyang 110016, China

ARTICLE INFO

Keywords:

Carbon nanotube
Aluminum matrix nanocomposite
Efficiency
Instability
Dynamic recrystallization

ABSTRACT

The determination of the optimum processing window of a material at elevated temperatures is essential for metal forming. Such an “ideal” processing window could be characterized by the workability parameters of power dissipation efficiency, Ziegler's instability criteria, and the presence of favorable microstructures. The purpose of the present study is to develop three-dimensional (3D) processing maps of a 2.0 wt% carbon nanotube (CNT) reinforced 2024Al nanocomposite and to manifest continuous changes of power dissipation efficiency and flow instability domains involving key processing parameters of temperature, strain rate, and strain via isothermal compressive tests. The optimal hot working parameters of the 2024Al base alloy and the 2.0 wt% CNT/2024Al nanocomposite were identified to be at higher temperatures and lower strain rates, with a moderately smaller processing window for the nanocomposite due to the strengthening effect of CNTs and microstructural complexities. Instability occurred at higher strain rates and lower temperatures for both base alloy and nanocomposite. In the stable domain dynamic recrystallization was observed to occur, and the fraction of recrystallized grains increased with increasing deformation temperature, along with the presence of more random textures.

1. Introduction

Carbon nanostructures, such as carbon nanotubes (CNTs), have been considered as effective reinforcements for metal matrix composites (MMCs) and have been the center of interest for several studies in the literature [1–4]. In addition to their lightweighting attribute, CNTs possess remarkable properties including ultra-high specific strength and stiffness [5–8]. To manufacture high-performance CNT-reinforced aluminum matrix composites (AMCs), it is necessary to establish a proper processing window via constructing material processing maps and identifying desirable microstructures. Some previous studies focused on the hot deformation behavior of lightweight alloys to control their forming process and obtain desired microstructures and mechanical properties. For instance, Gao et al. [9] studied the hot deformation behavior of a TA15 titanium alloy and observed the microstructural changes, where continuous dynamic recrystallization (CDRX) occurred. Similarly, Wang et al. [10] studied the main softening mechanisms of a 6061Al/B₄C composite via hot compression testing, and also observed the happening of dynamic recrystallization (DRX).

Processing maps are of special importance since they represent a powerful tool for identifying the optimal processing parameters during

manufacturing of materials at elevated temperatures. The design of new alloys relies heavily on hot working, and the relevant microstructural features are strongly influenced by thermo-mechanical processing parameters such as temperature, strain rate and strain during hot deformation [11,12]. Hence, through the development of processing maps, prevalent deformation mechanisms and microstructural features could be determined in different conditions. In this context, constitutive equations and processing maps were developed and presented in the literature for various alloys and composites such as Mg alloys [13–15], Al alloys [11,16–20], Cu alloys [21], high entropy alloys (HEAs) [12], Ni-based superalloys [22], Al6063/0.75Al₂O₃/0.75Y₂O₃ nanocomposite [23], 20 vol% S₂Cp/2024Al nanocomposite [24], and B₄C particulate-reinforced Al composite [18]. In addition to the conventional two-dimensional (2D) processing maps, some attempts were also made at a three-dimensional (3D) analysis of the safe (i.e., stable) processing window [17,25,26].

The advantage of 3D processing maps relative to the conventional 2D processing maps lies in the possibility of visualizing the “continuous” changes of power dissipation with respect to the processing parameters at the same time, rather than having to look at each processing map separately which might lead to a “discontinuity” in the

* Corresponding authors.

E-mail addresses: dchen@ryerson.ca (D.L. Chen), zya@imr.ac.cn (Z.Y. Ma).

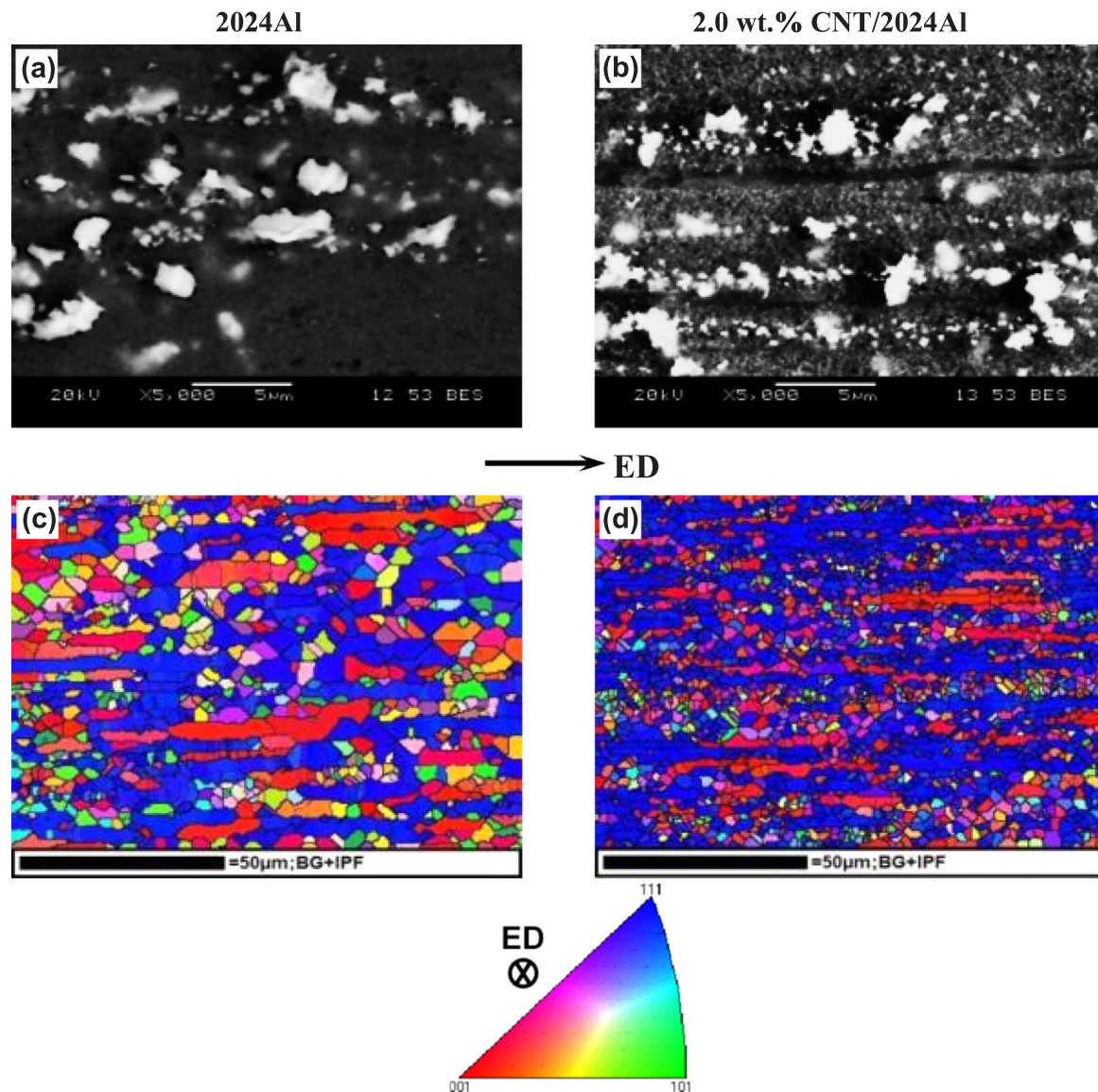


Fig. 1. Typical SEM micrographs showing the microstructural features and EBSD orientation maps of (a, c) the 2024Al alloy and (b, d) the 2.0 wt% CNT/2024Al nanocomposite, respectively. (For interpretation of the references to color in this figure, the reader is referred to the web version of this article).

observed results when comparing different maps at varying strain amounts. Hence, via the 3D processing maps it is easier to identify the local peaks of efficiency of power dissipation, so as to better choose the optimum processing parameters for hot working of materials. Metals like aluminum with high stacking fault energy might experience some difficulties in DRX during hot deformation. However, the presence of some alloying elements or reinforcements could alter the tendency to DRX [27]. DRX has indeed been observed to occur in the particulate- or whisker-reinforced AMCs [16,23,24,28], thus providing an opportunity to optimize the processing window and to achieve the desired post-deformation properties based on the evolution of microstructures.

Based on the brief literature review above, while different types of reinforcements have been studied for AMCs in terms of their hot workability and optimal processing windows, no information on 3D processing maps is available for the CNT-reinforced AMCs, to the best of the authors' knowledge. It is unclear how the CNT additions would influence the safe processing window and instability region of the composite and what impact this would have on the microstructural features such as DRX. Therefore, the present study was aimed to construct 3D processing maps of a 2.0 wt% CNT/2024 Al nanocomposite via isothermal compression up to 400 °C at different strain rates, while

emphasizing the underlying deformation mechanisms in the safe/stable processing regions via EBSD and XRD analyses. The effect of the addition of CNTs in the composite on the stable and unstable regions in relation to the thermo-mechanical processing parameters was also identified.

2. Experimental details

The studied nanocomposite consisted of 2.0 wt% CNTs mixed with 2024Al alloy powders having a composition (in wt%) of 4.5 Cu, 1.5 Mg, 0.6 Mn, and Al (balance). The average diameter of the 2024Al powders was ~ 10 μm. The as-received CNTs (95–98% purity) were synthesized using chemical vapor deposition (CVD). CNTs had entangled morphologies with a length of > 5 μm and an outer diameter of 10–20 nm. The as-mixed powders of 2024Al and 2.0 wt% CNTs were dispersed by ball milling for 6 h at a rotational speed of 400 rpm and a ball powder ratio of 15:1, using a stir milling machine with hardened steel balls of 5 mm in diameter. No extra pre-treatment was conducted on the CNTs before milling, however 2.0 wt% stearic acid was added to prevent serious cold-welding. The as-milled powders were cold-compacted in a cylinder die, degassed, then hot pressed at 560 °C for 1 h

into cylindrical billets. The as-pressed billets were hot extruded at 450 °C with a ratio of 25:1. The 2.0 wt% CNT/2024Al nanocomposite was finally solid solution-treated at 495 °C for two hours, quenched in water at RT and then naturally aged (i.e., in the T4 condition). Cylindrical specimens with a diameter of 5 mm and a height of 8 mm in concordance with ASTM E9-09 standard were prepared, with the compression axis parallel to the extrusion direction (ED). Compression tests were carried out until failure at 200 °C, 250 °C, 300 °C, 350 °C and 400 °C, at strain rates of 0.001, 0.01, and 0.1 s⁻¹, using a computerized United testing machine equipped with an environmental chamber having a temperature accuracy of ± 5 °C. Samples were first heated up to the deformation temperatures and held for 300 s in order to maintain a steady deformation temperature. A calibration curve at each temperature was obtained to get rid of the machine deformation in evaluating the stress-strain curves. To verify the reproducibility of the results, two tests were performed for each combination of strain rate and deformation temperature.

Scanning electron microscope (SEM) JSM-6380LV along with an Oxford energy dispersive X-ray spectroscopy (EDS) system was used to observe microstructures. EBSD analyses were carried out at a step size of 0.1 μm by means of Oxford integrated AZtecHKL advanced EBSD system with NordlysMax² and AZtecSynergy along with a large area analytical silicon drift detector. To characterize the initial microstructures, samples were polished via standard metallographic techniques. No etching was done for SEM investigations and the polished surfaces were examined directly. As for EBSD, sample surface was first mechanically polished, then electro-polished in an electrolyte of 10 ml nitric acid and 40 ml ethanol for about 30 s at 20 V and RT. Crystallographic texture was determined with a PANalytical X-ray diffractometer (XRD) with Cu K_α radiation at 45 kV and 40 mA in a back reflection mode by measuring partial pole figures (i.e., ranging between $\Psi = 0^\circ$ and 75°). The correction of the defocusing due to the rotation of XRD sample holder was made using the experimental data obtained from aluminum powder diffraction. Texture data obtained via XRD were subsequently evaluated using the Matlab-based MTEX software [29]. EBSD data were analyzed by means of the AZtecHKL EBSD data acquisition software of Oxford Instruments.

3. Results

3.1. Initial microstructural features

Fig. 1(a) and (b) present typical SEM micrographs of the 2024Al alloy and 2.0 wt% CNT/2024Al nanocomposite, respectively. Both micrographs indicate the presence of some coarser particles. A close examination of Fig. 1(b) revealed two types of particles which could be differentiated by their distinct size and shape, with one of them being uniformly-distributed nanoparticles in the Al matrix of the nanocomposite. These particles were identified in our previous studies via TEM [30,31] as singly-dispersed CNTs, which were shortened compared to the as-received ones due to the significant breakup during milling (i.e., the shear effect). As for the coarser particles in both Fig. 1(a) and (b) for the alloy and nanocomposite, they were revealed previously to be mainly Cu-containing Al₂Cu particles [30]. The presence of Al₂Cu particles was also acknowledged in the 5.0 wt% CNT-reinforced 2024Al nanocomposites [32]. Our previous XRD analysis and HRTEM examination on the nanocomposite [30,31] also revealed the presence of the aluminum carbide Al₄C₃ being either directly attached to CNTs or in the matrix in the vicinity of CNTs. Some coherent interfaces between CNTs and matrix were also observed, which played a major role in the direct bonding between the matrix and reinforcement (i.e., load transfer effect [30,33]).

Fig. 1(c) and (d) display EBSD orientation maps for the 2024Al alloy and 2.0 wt% CNT/2024Al nanocomposite, respectively, where the map color legend was projected towards the ED. Larger elongated grains in both alloy and nanocomposite mainly exhibited a <111> orientation

(blue color), with some elongated grains orientated in the <001> direction (red color). Equiaxed grains present in Fig. 1(c) and (d) exhibited more randomized orientations or assorted colors. Likewise, EBSD maps of a laminated CNT/7055Al nanocomposite were studied in [34] and the presence of a strong <111> fiber texture was reported. In fact, this orientation was acknowledged as a hard orientation in the face-centered cubic (FCC) structures, in direct relation to the normal {111}<110> slip systems [35]. Elongated grains in Fig. 1(c) and (d) along the ED were credited to the severe plastic deformation during extrusion since microstructural features are highly dependent on the deformation process [36]. As seen from Fig. 1(c) and (d), grain refinement was achieved due to the presence of CNTs in the nanocomposite. Similarly, SiC particles were also reported to reduce grain sizes of 2024Al matrix [37]. The grain refinement in MMCs due to CNT additions was also observed in [38,39]. Second-phase particles observed in Fig. 1(a) and (b) (i.e., nano-sized CNTs and Cu-containing particles) played a significant role in controlling grain sizes via stimulating the nucleation of recrystallization and pinning grain boundaries (GBs) [40]. A force related to the size of particles and the energy of GBs was required to move a boundary beyond a particle [41]. In the present nanocomposite, the CNTs would cause a strong “motion restriction” of GBs by acting as strong pinning forces (i.e., the frictional forces to the moving of GBs [38]), effectively prohibiting the grain growth and therefore leading to grain refinement as observed in Fig. 1(d).

3.2. Flow behavior

Fig. 2(a) and (b) present the change of the compressive yield strength (CYS) as a function of both temperature and strain rate via 3D surface plots for the 2024Al and the 2.0 wt% CNT/2024Al, respectively. The main advantage of such 3D surface plots lay in preserving the continuity of results when transitioning between various test conditions. Obviously, a decrease in temperature and an increase in the strain rate led to increasing CYS values. While a similar trend was observed for both the alloy and nanocomposite, the overall CYS was higher for the nanocomposite at a given deformation temperature and strain rate. Thus, the strengthening role of CNTs in the nanocomposite was clearly demonstrated. This was mainly attributed to the judicious composite effect exerted by the well-dispersed CNTs along with the Hall-Petch strengthening mechanism (i.e., the GB strengthening), where the material gains in strength by refining its average grain size due to increasing interactions between dislocations and GBs. The motion of dislocations during deformation was impeded by GBs to form dislocation pile-ups owing to the presence of barriers caused by the misorientations between neighboring grains. Grain refinement in the present nanocomposite could be seen in Fig. 1(d) in comparison with Fig. 1(c). Thus, the smaller the grain size is, the more GBs are present, leading to a more difficult dislocation movement and thus a higher flow stress. Similar grain refinement observations and the related increase in the deformation resistance were also reported in [42–44]. As also seen from Fig. 2, while both alloy and nanocomposite exhibited lower CYS values at higher temperatures, a better response was observed for the nanocomposite. This could be attributed to the augmented thermal activation and the kinetic energy of metal matrix which boosted the dislocation movements at elevated temperatures [45]. It is also noted that the compressive behavior of the present 2024Al base alloy was highly improved (i.e., before being further enhanced by CNT additions) in comparison with the conventional wrought 2024Al alloy in T4 condition [46]. Various factors might have contributed to this enhancement, mainly ball milling, which has resulted in a more refined microstructure in conjunction with a likely increase of dislocation density arising from the high-energy collision from the balls. The effect of milling time on the mechanical properties of a pure Al was examined by Choi et al. [42], who reported that the YS of the unmilled Al (~60 MPa) could be elevated to higher values due to milling. For different milling times, the following YS values were reported: ~210 MPa after

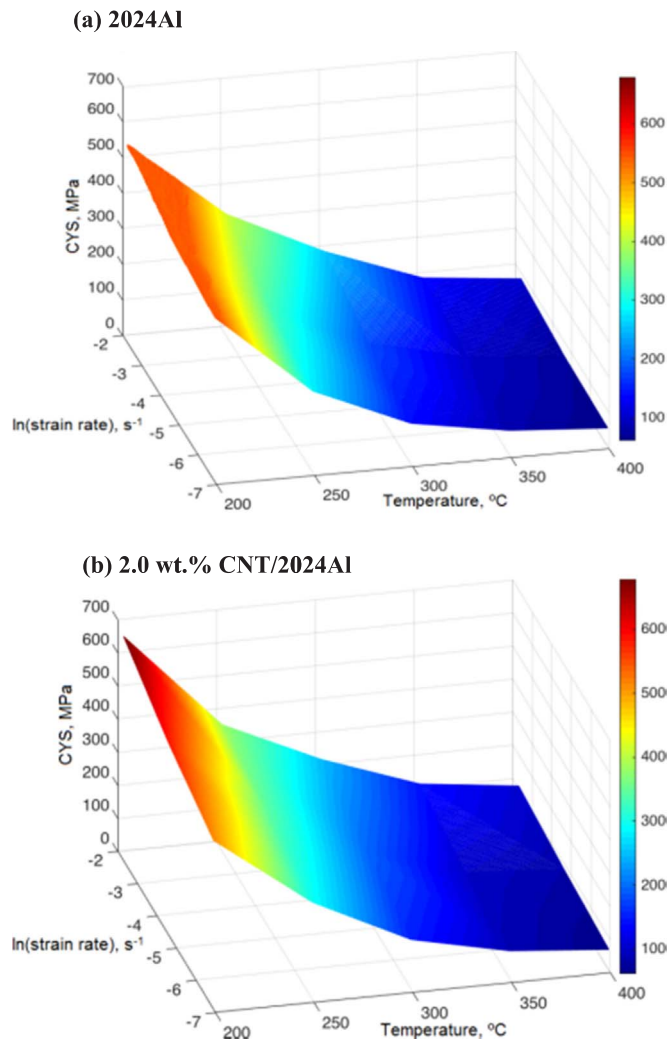


Fig. 2. Three-dimensional (3D) surface plot showing the changes of compressive yield strength (CYS) with deformation temperature and ln (strain rate) of (a) the 2024Al alloy, and (b) the 2.0 wt% CNT/2024Al nanocomposite.

6 h, ~ 250 MPa after 12 h, ~ 300 MPa after 18 h, and ~ 380 MPa after 24 h. The effective improvement of YS between the milled and unmilled Al, even for the shortest milling times could be explained by the major grain refinement credited to the Hall-Petch effect. Another reason for the improvement of the mechanical properties in both alloy and nanocomposite, which could be linked to the fabrication process as well, was the spontaneous reaction between Al and O₂ when exposed to air during milling of 2024Al powders. The formed Al₂O₃ particles were then dispersed in the 2024Al matrix after extrusion, leading to an additional increase in the strength via the Orowan strengthening mechanism [30,31,47,48]. Naturally, the addition of CNTs and the presence of Al₂Cu particles played an important role in strengthening the nanocomposite via a number of mechanisms, including load transfer, thermal mismatch, Orowan looping, and Zener drag effect [30,31,47].

3.3. Processing maps

3.3.1. Basis of processing maps

Processing maps represent the most effective alternative for determining the optimal hot workability regions of materials. The concept of processing maps relies on the dynamic material model (DMM) [17,19,25], according to which the workpiece dissipates power during hot deformation and the constitutive response of the material at a given temperature depends essentially on strain rate and to a lesser extent on strain [14]. The total power per unit volume P absorbed by the

workpiece during plastic flow may be expressed as a sum of two complementary terms [15],

$$P = G + J = \int_0^{\dot{\epsilon}} \sigma d\dot{\epsilon} + \int_0^{\sigma} \dot{\epsilon} d\sigma, \quad (1)$$

where G represents the power dissipated by plastic deformation, most of which is converted into heat, and J represents the dissipation through microstructure evolution (e.g., dynamic recovery, dynamic recrystallization, superplastic flow, phase transformation, crack propagation). At any given temperature and strain, the partitioning of power between J and G is given by [14],

$$\frac{dJ}{dG} = \frac{\partial \ln \sigma}{\partial \ln \dot{\epsilon}} = m, \quad (2)$$

where m is the strain rate sensitivity of the material. Knowing the values of m , dissipation through the microstructure evolution J may be normalized with respect to J_{max} to obtain a dimensionless parameter called the efficiency of power dissipation [25], i.e.,

$$\eta = \frac{J}{J_{max}} = \frac{2m}{m+1}. \quad (3)$$

The change of η with temperature and strain rate reveals the features of power dissipation arising from microstructural changes in the workpiece, creating the power dissipation map. This map could be presented as contour plots of efficiency change in the temperature-strain rate domain where different regions (i.e., corresponding to different η values) signify different deformation mechanisms. A continuum instability criterion, obtained based on the extremum principles of irreversible thermodynamics, could also be provided as [20],

$$\xi(\dot{\epsilon}) = \frac{\partial \ln(m/m+1)}{\partial \ln \dot{\epsilon}} + m < 0. \quad (4)$$

The instability parameter $\xi(\dot{\epsilon})$ in Eq. (4) could be used to mark out the flow instability regions after being evaluated as a function of temperature and strain rate. The instability map was obtained when $\xi(\dot{\epsilon}) < 0$, representing the occurrence of flow instability. With the values of η and $\xi(\dot{\epsilon})$ at different temperatures, strain rates and strains, processing maps can be established by superimposing the instability maps over the power dissipation maps. Conventional 2D maps along with 3D processing maps will be analyzed in the coming sub-sections.

As mentioned above, the processing maps were built on the basis of a series of isothermal compression tests performed at different strain rates and temperatures while fixing the strain amount each time. Two tests were also conducted in each condition to ensure the reproducibility of the results. Once all the data in different conditions were collected and η and $\xi(\dot{\epsilon})$ values were calculated, Matlab curve fitting toolbox was used to achieve a higher resolution of the processing maps. Using this toolbox, it is possible to fit a surface of the form $v = f(x, y)$ to the data in the vectors (x, y, v) . The arrays of data obtained during the experiment are then interpolated and specific query points (x_q, y_q) , as labeled in the Matlab terminology, are specified. The interpolated values v_q are then returned and the new surface is obtained knowing that it would always pass through the initial (i.e., experimental) data points defined by the x and y arrays, as the only purpose of the fitting is to achieve higher resolution and better looking images within the margins defined by the experimental data. The further details needed to construct the 3D processing maps and their advantage will be addressed below in the designated sub-sections.

3.3.2. Conventional 2D processing maps

Fig. 3(a)–(c) show the 2D processing maps of the 2024Al obtained at strain values of 0.1, 0.3, and 0.5, respectively. The same strain values were chosen for the 2D processing maps of 2.0 wt% CNT/2024Al in Fig. 4(a)–(c). The colored areas in Figs. 3 and 4 separated by contour lines designate the degree of efficiency (i.e., the η values calculated based on Eq. (3)). The limit of the highest efficiency region in each map

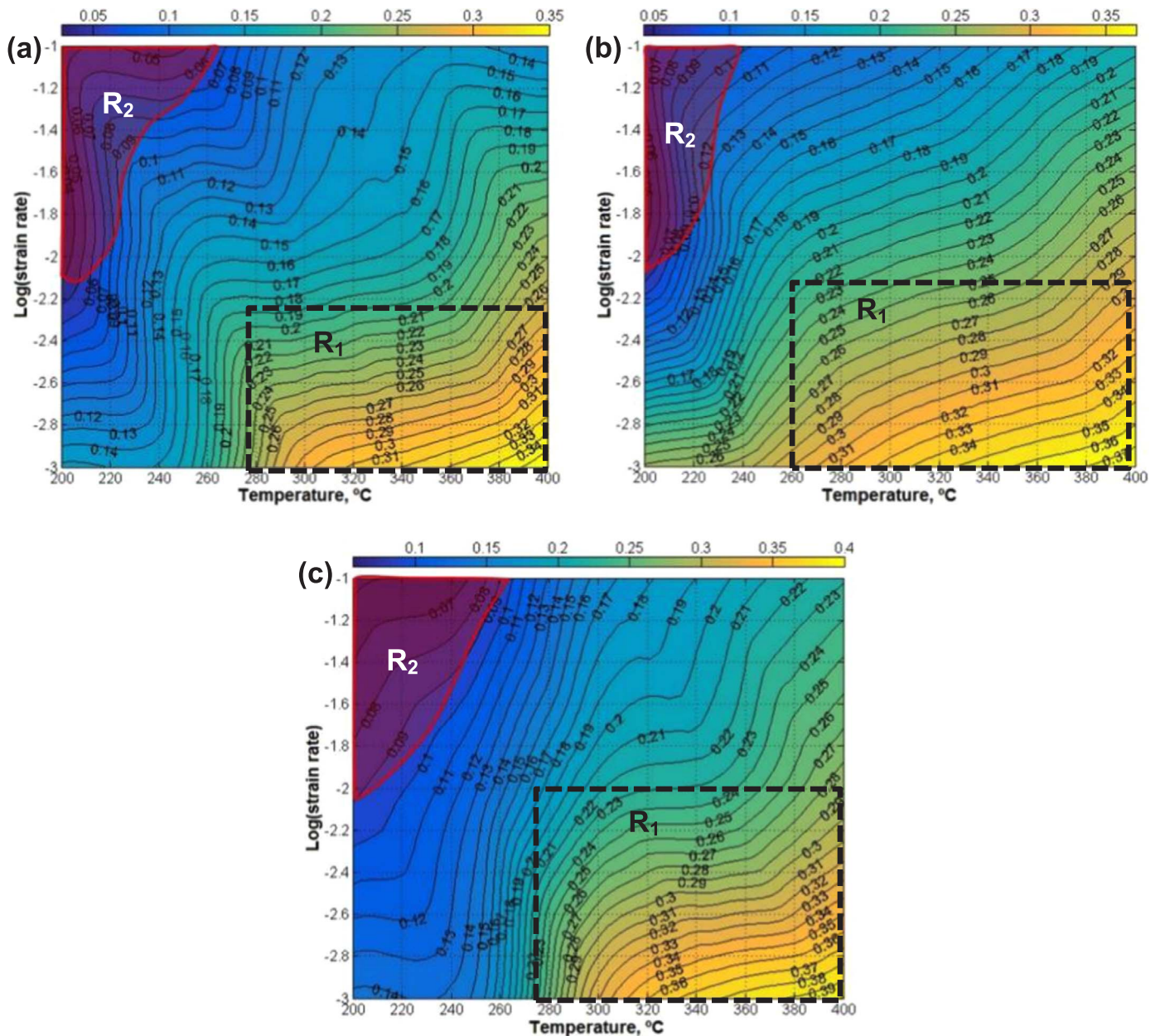


Fig. 3. Processing maps of the 2024Al alloy at a true strain of (a) $\epsilon = 0.1$, (b) $\epsilon = 0.3$, and (c) $\epsilon = 0.5$, respectively. (For interpretation of the references to color in this figure, the reader is referred to the web version of this article).

was approximated by the dashed boxes, i.e., indicated by R_1 in Figs. 3 and 4. The highlighted regions R_2 denoted the flow instability domains plotted based on Eq. (4). The peak efficiency values showed a slight variation from one map to the other for both materials. For instance, for the 2024Al, the peak value of η varied from $\sim 35\%$ at $\epsilon = 0.1$, to $\sim 37\%$ at $\epsilon = 0.3$, to $\sim 39\%$ at $\epsilon = 0.5$. A similar variation of the maximum η values was also reported in [19] for the 2024Al alloy, from $\sim 39\%$ at $\epsilon = 0.1$, to $\sim 44\%$ at $\epsilon = 0.3$, to $\sim 46\%$ at $\epsilon = 0.5$. The larger η values in [19] than the current ones could be related to their higher upper temperature limit of $500\text{ }^\circ\text{C}$, compared with $400\text{ }^\circ\text{C}$ in the present work. Also, the fabrication process, where samples of as-cast 2024Al were studied in [19], could have played a role. Efficiency was also reported to increase with increasing strain in [25]. A similar trend was observed for the nanocomposite in Fig. 4 as well ($\eta \sim 27\%$ at $\epsilon = 0.1$, $\sim 29\%$ at $\epsilon = 0.3$, and $\sim 30\%$ at $\epsilon = 0.5$).

The stable domains with fairly high values of efficiency (R_1 Figs. 3 and 4) corresponded to the deformation at higher temperatures and lower strain rates. On the other hand, the flow instability domains R_2

corresponded to lower temperatures and higher strain rates. Limits of R_1 also varied with strain for both alloy and nanocomposite. For the 2024Al, it went from $280\text{--}400\text{ }^\circ\text{C}/0.001\text{--}0.006\text{ s}^{-1}$ at $\epsilon = 0.1$, to $260\text{--}400\text{ }^\circ\text{C}/0.001\text{--}0.008\text{ s}^{-1}$ at $\epsilon = 0.3$, and $275\text{--}400\text{ }^\circ\text{C}/0.001\text{--}0.01\text{ s}^{-1}$ for $\epsilon = 0.5$. As for the nanocomposite in Fig. 4, R_1 changed with strain: $303\text{--}400\text{ }^\circ\text{C}/0.001\text{--}0.01\text{ s}^{-1}$ at $\epsilon = 0.1$, $280\text{--}400\text{ }^\circ\text{C}/0.001\text{--}0.006\text{ s}^{-1}$ at $\epsilon = 0.3$, and $285\text{--}400\text{ }^\circ\text{C}/0.001\text{--}0.009\text{ s}^{-1}$ at $\epsilon = 0.5$. Instability region R_2 also varied moderately with strain in both materials. By comparing the extent of each of the regions between the alloy and the nanocomposite, the “safe” (i.e., stable) window was observed to relatively shrink for the nanocomposite. This was expected since the structural complexity introduced by CNTs led to the restriction of the working window, demanding a tighter process control. Likewise, Malas et al. [28] studied the difference of the optimum processing windows between a P/M-2024Al and a P/M-2024Al reinforced with 20 v/o SiC_w . They reported that the safe processing for the composite occurred over a narrower range of temperature and strain rate, which was associated with the presence of

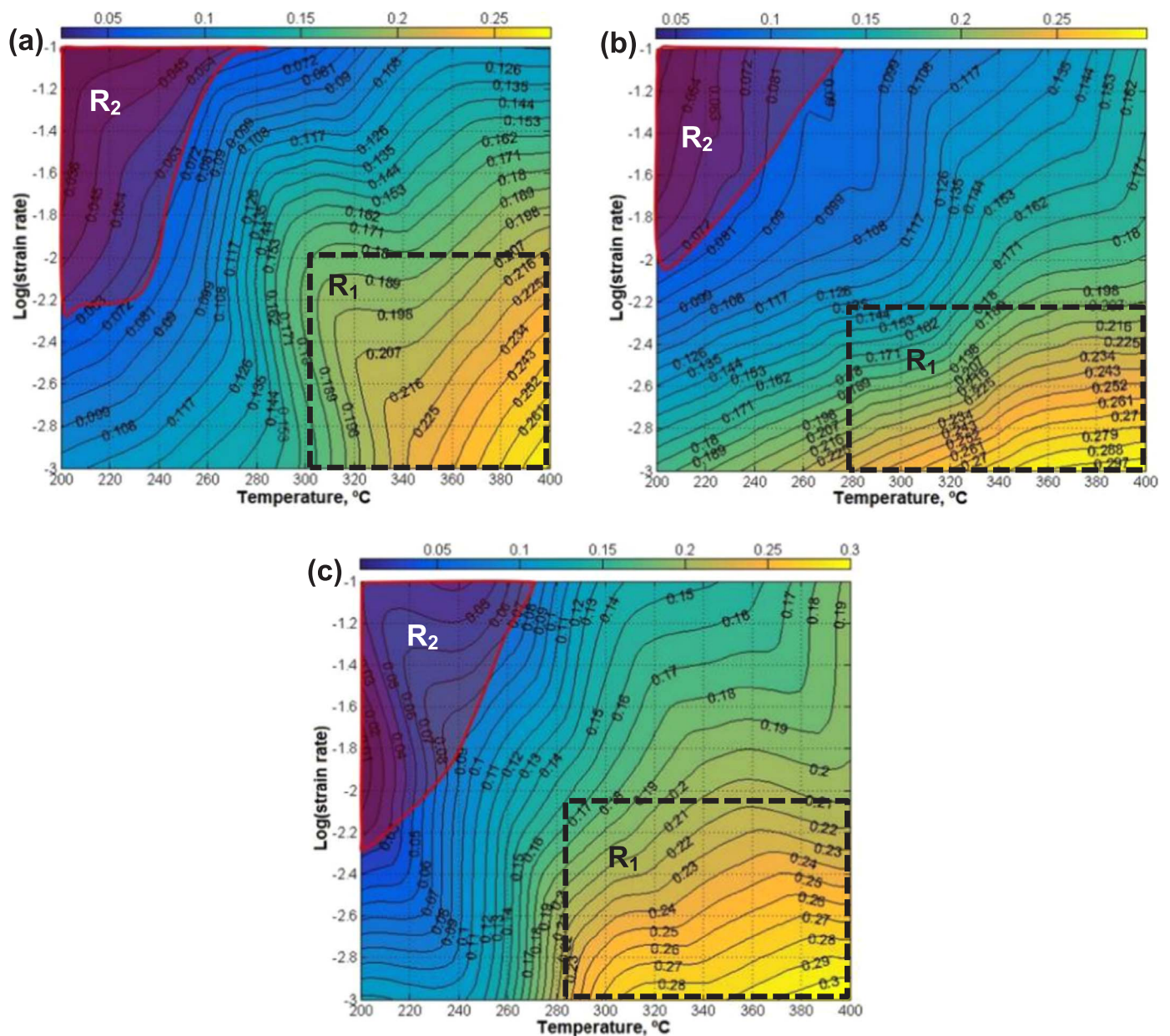


Fig. 4. Processing maps of the 2.0 wt% CNT/2024Al nanocomposite at a true strain of (a) $\varepsilon = 0.1$, (b) $\varepsilon = 0.3$, and (c) $\varepsilon = 0.5$, respectively. (For interpretation of the references to color in this figure, the reader is referred to the web version of this article).

reinforcement (being a rigid ceramic phase in a plastically-deformed matrix), risking cavitation, and whisker fracture at lower temperatures. Similar results on the safe regions of an A356 alloy and an A356 reinforced with 5 wt% B₄C composite were reported in [18], where the maximum efficiency region was observed to be smaller for the nanocomposite as well, which reflected the impact of reinforcement. The effect of the fabrication process was also considered in [28], where wrought 2024Al showed a wider processing window than ingot 2024Al due to homogenization and reconstitution of the microstructure as a result of prior thermomechanical treatment.

Whether it is the reinforcement or the addition of alloying elements, a change introduced to the base alloy would affect its optimum processing window. In this context, the 7150Al base alloy reported in [16] witnessed single stable domains at fixed strains like the case of the 2024Al in Fig. 3. A peak efficiency of 42% at 450 °C and 0.01 s⁻¹ was first achieved in the 7150Al base alloy. Then, when higher Zr contents (0.12–0.15%) were added to the alloy, the precipitation of Al₃Zr dispersoids influenced the processing maps. The safe domain appeared to

shrink toward higher temperatures and higher strain rates [16]. This was similar to the present work (303–400 °C/0.001–0.01 s⁻¹) (Fig. 4(a)) in comparison with Fig. 3(a) (280–400 °C/0.001–0.006 s⁻¹). A decrease in the efficiency values was also reported after adding Zr element in the 7150Al alloy, similar to the present alloy and nanocomposite (i.e., $\eta_{\max} \sim 35\%$ in Fig. 3(a), and $\sim 27\%$ in Fig. 4(a)). At different strains in [16], safe domains narrowed down when increasing temperatures and decreasing strain rates, and flow instability regions expanded toward lower strain rates, being also similar to the characteristics of the present alloy in Fig. 3(b) (260–400 °C/0.001–0.008 s⁻¹ vs. 280–400 °C/0.001–0.006 s⁻¹), and the nanocomposite in Fig. 4(b) and (c) (275–400 °C/0.001–0.01 s⁻¹ vs. 285–400 °C/0.001–0.009 s⁻¹). It should be noted that, in addition to the safe domains positioned at higher temperatures lower strain rates, a second stable domain was observed in [19] in the range of 250–300 °C and 10–100 s⁻¹. Since such high strain rates could not be obtained in the current study, the existence of the second stability window could not be verified. In an Al6063/0.75Al₂O₃/0.75Y₂O₃ nanocomposite, the

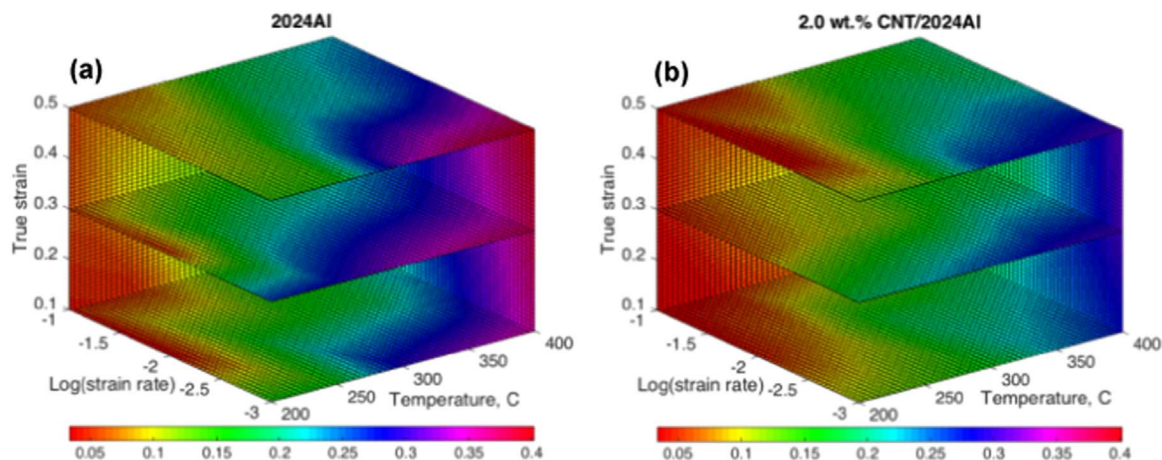


Fig. 5. 3D power dissipation maps of (a) the 2024Al alloy and (b) the 2.0 wt% CNT/2024Al nanocomposite sliced at a true strain of $\varepsilon = 0.1$, $\varepsilon = 0.3$, and $\varepsilon = 0.5$, respectively. (For interpretation of the references to color in this figure, the reader is referred to the web version of this article).

optimum processing domains for hot working were also observed to be positioned only at high temperatures and low strain rates [23], which was similar to the situation of the studied materials.

3.3.3. 3D processing maps

Based on the 2D processing maps in Figs. 3 and 4, some differences were noted with respect to strain values. However, plotting the processing maps in this traditional way does not allow the contemplation of the effect of strain continuously since the maps are shown separately at each strain. Thus, it would be better to depict the evolution of the processing parameters during deformation in a continuous manner. This could be achieved by plotting 3D processing maps and flow instability maps which were developed for the alloy and nanocomposite in Figs. 5–8. Such a representation has the advantage of identifying the safe hot processing conditions of the whole deformation process directly, which is more convenient when observing the behavior of a specific material. This technique was previously used in [25] for an AZ31B Mg alloy and in [17] for an AA7050 alloy. An attempt to construct a 4D processing map was also introduced in [19] for a 2024Al alloy.

In the present study, 3D power dissipation maps were constructed while introducing “slices” at chosen values of one of the parameters (i.e., ε in Fig. 5, T in Fig. 6, and $\dot{\varepsilon}$ in Fig. 7). Obtaining these plots not only satisfies representation purposes, but also helps display specifically targeted planes (i.e., at designated values of any of the process parameters) through the volumetric set of data by creating a “slice surface” in the domain of the volume. Not only does this feature allow a clear 3D

representation based on the fitted experimental data, but also it allows a “cut-through” view so as to see a combined effect of all process parameters as well as the effect of a designated one among them along the different slices. Fig. 5(a) and (b) illustrate the 3D power dissipation maps of the 2024Al and the 2.0 wt% CNT/2024Al sliced at $\varepsilon = 0.1$, $\varepsilon = 0.3$, and $\varepsilon = 0.5$, respectively. The effect of strain on the efficiency of power dissipation η could be seen vertically in Fig. 5 through the variation of the grid levels, which proved that η varied reasonably with increasing strain. The higher η values of the base alloy relative to the nanocomposite were well appreciated through the change of color flow in Fig. 5. Fig. 6(a) and (b) present the second slicing option based on the temperature values for the alloy and nanocomposite, respectively. Three representative temperatures of 200, 300, and 400 °C were chosen. The η increased with increasing temperature for both materials, with a higher value for the alloy. At each chosen temperature, η displayed an increasing value towards lower strain rates. Fig. 7(a) and (b) demonstrate the effect of strain rate on the efficiency values sliced at 0.001, 0.01, and 0.1 s^{-1} . η clearly increased with decreasing strain rate for both materials. In Fig. 7(a) for the 2024Al, at the lowest strain rate of 0.001 s^{-1} two different regions could be identified, which could not be seen in the 2D maps of Fig. 3. Thus, the 3D representation helps gather more information on the behavior of the material. As seen from Fig. 7(a), η values of $\sim 20\%$ were seen at higher and lower strains and at a lower temperature range (200–275 °C), indicating the effect of strain on the processing maps. These two regions also appeared for the nanocomposite to some extent. Based on the high efficiency regions in Figs. 5–7, one could infer that the favorable conditions for hot

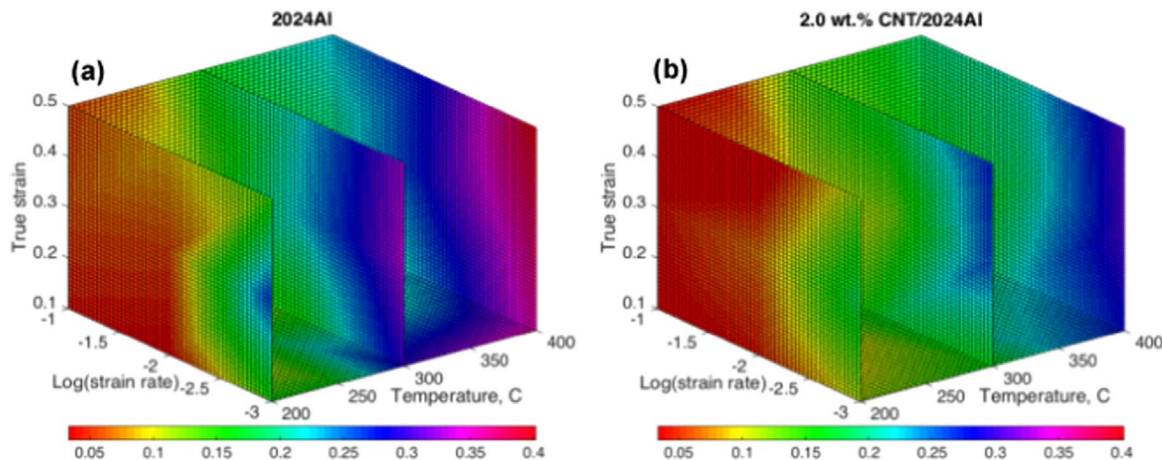


Fig. 6. 3D power dissipation maps of (a) the 2024Al alloy and (b) the 2.0 wt% CNT/2024Al nanocomposite sliced at a temperature of 200, 300, and 400 °C, respectively.

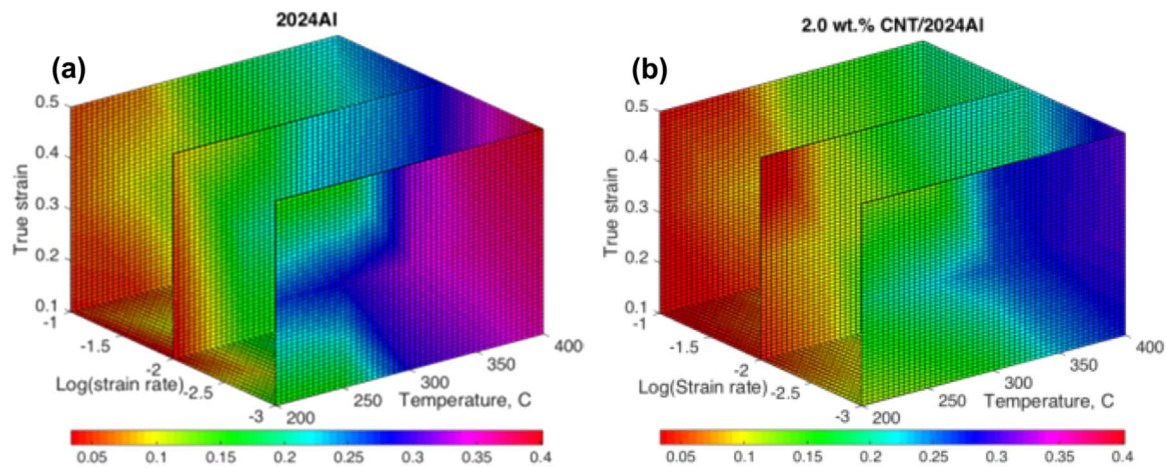


Fig. 7. 3D power dissipation maps of (a) the 2024Al alloy and (b) the 2.0 wt% CNT/2024Al nanocomposite sliced at a strain rate of 0.001 s^{-1} ($\log(\dot{\epsilon}) = -3$), 0.01 s^{-1} ($\log(\dot{\epsilon}) = -2$), and 0.1 s^{-1} ($\log(\dot{\epsilon}) = -1$), respectively.

processing remained in the regions of higher temperatures and lower strain rates, since the domains with a higher efficiency of power dissipation commonly represented the optimum processing conditions [11].

3D flow instability maps were also generated for the alloy and nanocomposite while considering only higher strain rate regions in-between 0.01 and 0.1 s^{-1} based on Figs. 3 and 4. Larger instable regions were observed for the nanocomposite at all the chosen strain rates. Most negative ξ values were seen around the applied lower temperature limit (i.e., $\sim 200 \text{ }^\circ\text{C}$) in Fig. 8(a). A bigger region of flow instability was noted for the nanocomposite, where the most negative ξ values appeared at 0.1 s^{-1} (Fig. 8(b)). The instability region almost vanished at 0.01 s^{-1} for the alloy. The 3D instability maps suggested that the hot workability of the alloy and nanocomposite became inferior as the strain rate increased, i.e., it became progressively difficult to deform the alloy and nanocomposite at higher strain rates. It is generally accepted that flow instability was associated with the localized shear initiated by high strain rates [14].

4. Discussion

Throughout the literature, the microstructures related to safe (i.e., stable) domains have been attributed to dynamic recovery (DRV), dynamic recrystallization (DRX) and superplasticity, depending on the materials [25]. Several studies were reported in this context. For instance, a similar 2024Al alloy was studied by Malas et al. [28] and DRX

was reported at lower strain rates starting from $250 \text{ }^\circ\text{C}$. Generally, the peak value of η reflecting the occurrence of DRX in the Al alloys was ranged from 35% to 50% [24], which is in agreement with the present 2024Al as shown in Fig. 3 ($\sim 35\%$ at $\epsilon = 0.1$, $\sim 37\%$ at $\epsilon = 0.3$, and $\sim 39\%$ at $\epsilon = 0.5$). However, the peak value of η was reported to decrease in the AMCs, which also conformed well to the findings in Fig. 4. This observation could be attributed to the increase of power dissipated by plastic work during hot deformation for the AMCs, since they admit a larger number of fine reinforcing particles which would potentially raise their flow stress [24].

Based on the information provided above, the purpose of this section is to observe the deformed microstructures and textures in the stable domains while comparing them to the initial features observed prior to deformation in Fig. 1. Such a discussion would help understand the microstructural and textural mechanisms that played a role in distinguishing the safe hot working windows for the 2024Al alloy and 2.0 wt% CNT/2024Al composite. Since these safe windows were identified to be positioned at higher temperatures and lower strain rates for both alloy and composite, the deformed microstructures and crystallographic textures were analyzed at 300, 350, and $400 \text{ }^\circ\text{C}$ and at a fixed strain rate of 0.001 s^{-1} . EBSD analyses were conducted for the 2024Al, while XRD analyses were performed for the nanocomposite, since it was challenging to obtain accurate EBSD results of MMCs [49–51], especially after plastic deformation due to the poor fit of the solution to the pattern (i.e., with large mean angular deviation (MAD) values [52]). The importance of the EBSD analysis and the XRD pole figures that will

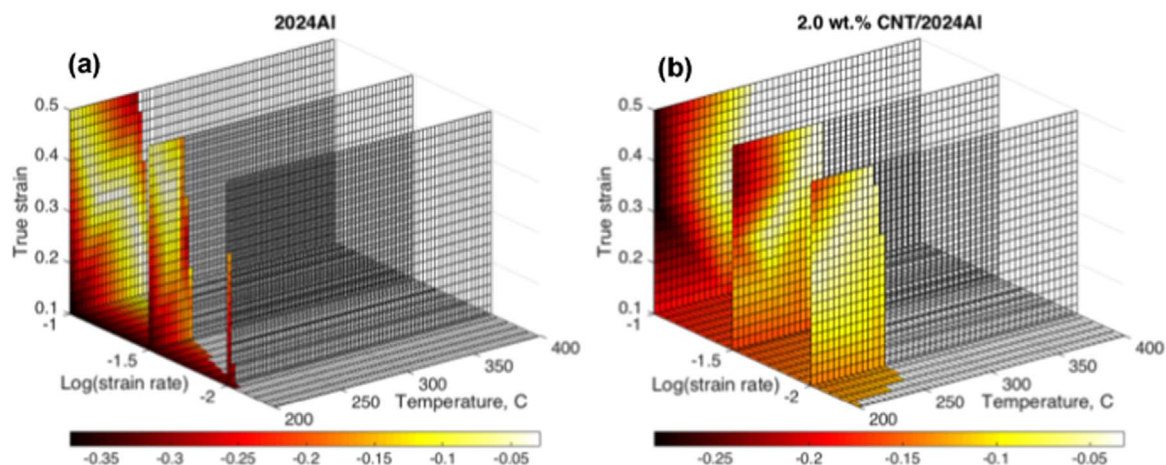


Fig. 8. 3D flow instability maps of (a) the 2024Al alloy and (b) the 2.0 wt% CNT/2024Al nanocomposite sliced at a strain rate of 0.01 s^{-1} ($\log(\dot{\epsilon}) = -2$), 0.03 s^{-1} ($\log(\dot{\epsilon}) = -1.5$), and 0.1 s^{-1} ($\log(\dot{\epsilon}) = -1$), respectively.

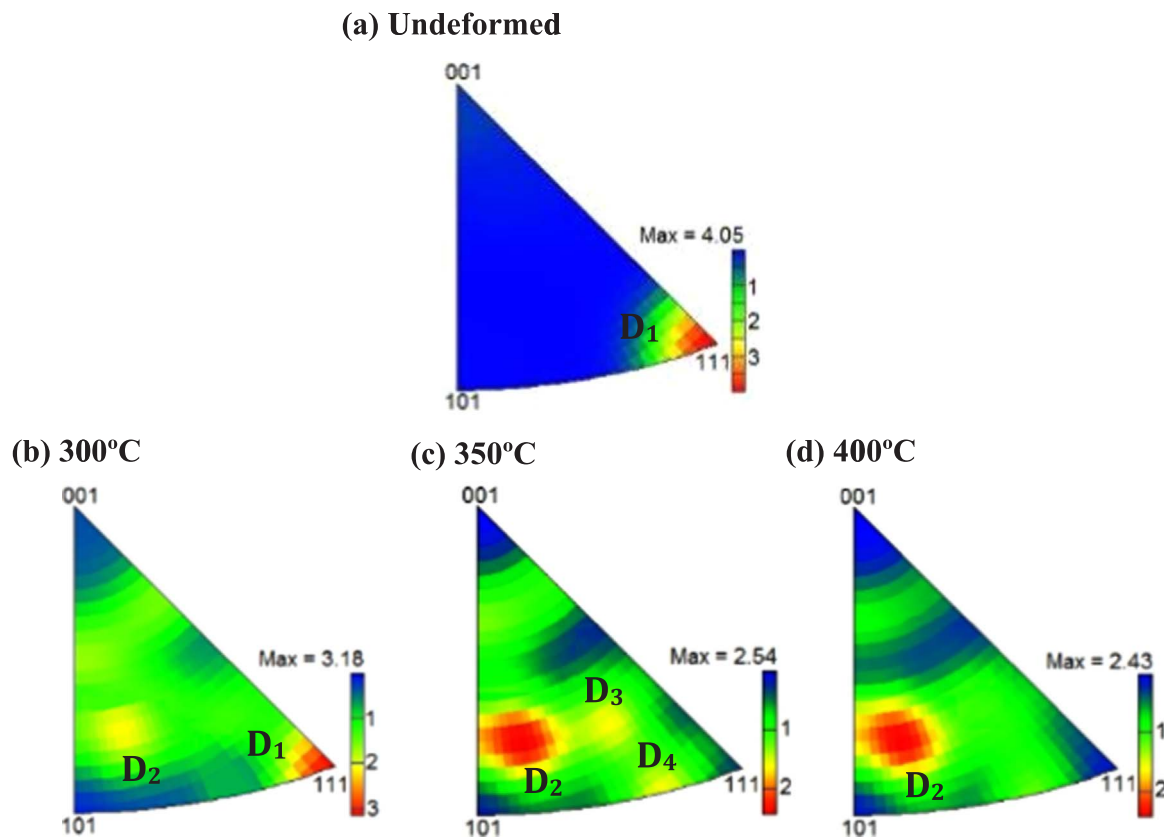


Fig. 9. EBSD inverse pole figures of the 2024Al alloy (a) undeformed, and deformed at (b) 300 °C, (c) 350 °C, and (d) 400 °C at a strain rate of 0.001 s⁻¹.

be discussed throughout this section lies in their ability to depict the behavior of the material from the lower limit of the stable region to the upper limit which is characterized by the highest η values. Texture components by means of EBSD inverse pole figures (IPFs) and XRD pole figures will also be identified, in addition to the study of the recrystallized fraction component maps.

IPFs reflecting the orientation components developed in the 2024Al alloy were presented in Fig. 9. At the initial stage, prior to deformation, a maximum intensity of 4.05 MRD (multiples of a random distribution) was observed at the location D_1 (Fig. 9(a)). This confirms that the majority of the grains were initially parallel to $\langle 111 \rangle$. After hot compression at 300 °C (Fig. 9(b)), the $\langle 111 \rangle$ -oriented component became weaker with a maximum intensity of ~ 3.2 MRD and the formation of a new faint component D_2 was detected. When the deformation temperature increased to 350 °C, the corresponding IPF revealed a more random orientation in the absence of the previous D_1 (or $\langle 111 \rangle$ component), with a maximum density of ~ 2.5 MRD for D_2 and faint transient positions D_3 and D_4 (Fig. 9(c)). At a deformation temperature of 400 °C, D_2 persisted with only a slightly lower density of ~ 2.4 MRD (Fig. 9(d)). Thus, D_2 could be considered as a “DRX texture component” for the 2024Al alloy.

The recrystallized fraction of the specimens deformed in the safe region via EBSD analyses is shown in Fig. 10(a), (c) and (e) for 300, 350, and 400 °C, respectively, along with their corresponding quantification histograms shown in Fig. 10(b), (d) and (f). By means of EBSD, it is possible to distinguish recrystallized grains from deformed ones based on the internal statistics of the grains. It is known that for a deformed grain, the dislocation density is high and dislocations are arranged in substructures, which result in local misorientations of several degrees within the grains [53]. In contrast, recrystallized grains have much lower dislocation densities, thus, the grain internal statistical information can be used to identify the nature of the grains. One method is to determine the overall spread in orientations within a grain, i.e., by obtaining the grain orientation spread (GOS). For a given grain,

GOS is the average deviation between the orientation of each point (or pixel) within the grain and the average orientation of the entire grain. GOS values of recrystallized grains are lower than those of deformed grains and a threshold value is required to differentiate recrystallized grains among others. In the present study, a “recrystallized” grain was set to have a GOS value of $< \sim 2^\circ$, while a grain marked to be “sub-structured” had a GOS value in-between 2° and 5° . When the GOS value was $> 5^\circ$, the grain was labeled as “deformed”. As seen from Fig. 10, the recrystallized grain fraction increased with increasing deformation temperature. While the increase from 300 to 350 °C was only $\sim 2\%$, a significant gain in the recrystallized fraction occurred from 350 to 400 °C with a $\sim 8\%$ increase. This was expected since a maximum efficiency of power dissipation of $\sim 39\%$ was attained at 400 °C and 0.001 s⁻¹, introducing a more homogenized microstructure due to DRX. These observations were in agreement with those reported in [28], where DRX occurred above 250 °C at lower strain rates. Also, the 2024Al exhibited fine equiaxed grains with no significant grain growth below a deformation temperature of 425 °C, and abnormal grain growth occurred beyond a temperature of 482 °C [28]. This limit was much higher than our highest deformation temperature of 400 °C. As a result, continuous DRX was essentially present where new grains nucleated evenly at high temperatures and low strain rates. Indeed, for the metals with high stacking fault energy (e.g., Al alloys), the main mechanism for DRX is continuous dynamic recrystallization (CDRX) at higher deformation temperatures [54], and the new grains could be formed by transforming the low-angle grain boundaries to high-angle grain boundaries. Therefore, the peak efficiency of power dissipation may be mainly attributed to grain refinement by CDRX.

In order to understand the evolution of the crystallographic texture in the composite within the optimal processing window, $\{110\}$ pole figures at consecutive deformation stages were analyzed in comparison with the initial $\{110\}$ pole figure prior to deformation (Fig. 11(a)). Initially, the majority of $\{110\}$ poles were aligned parallel to RD with a maximum intensity of ~ 4.4 MRD located at component P_1 . After

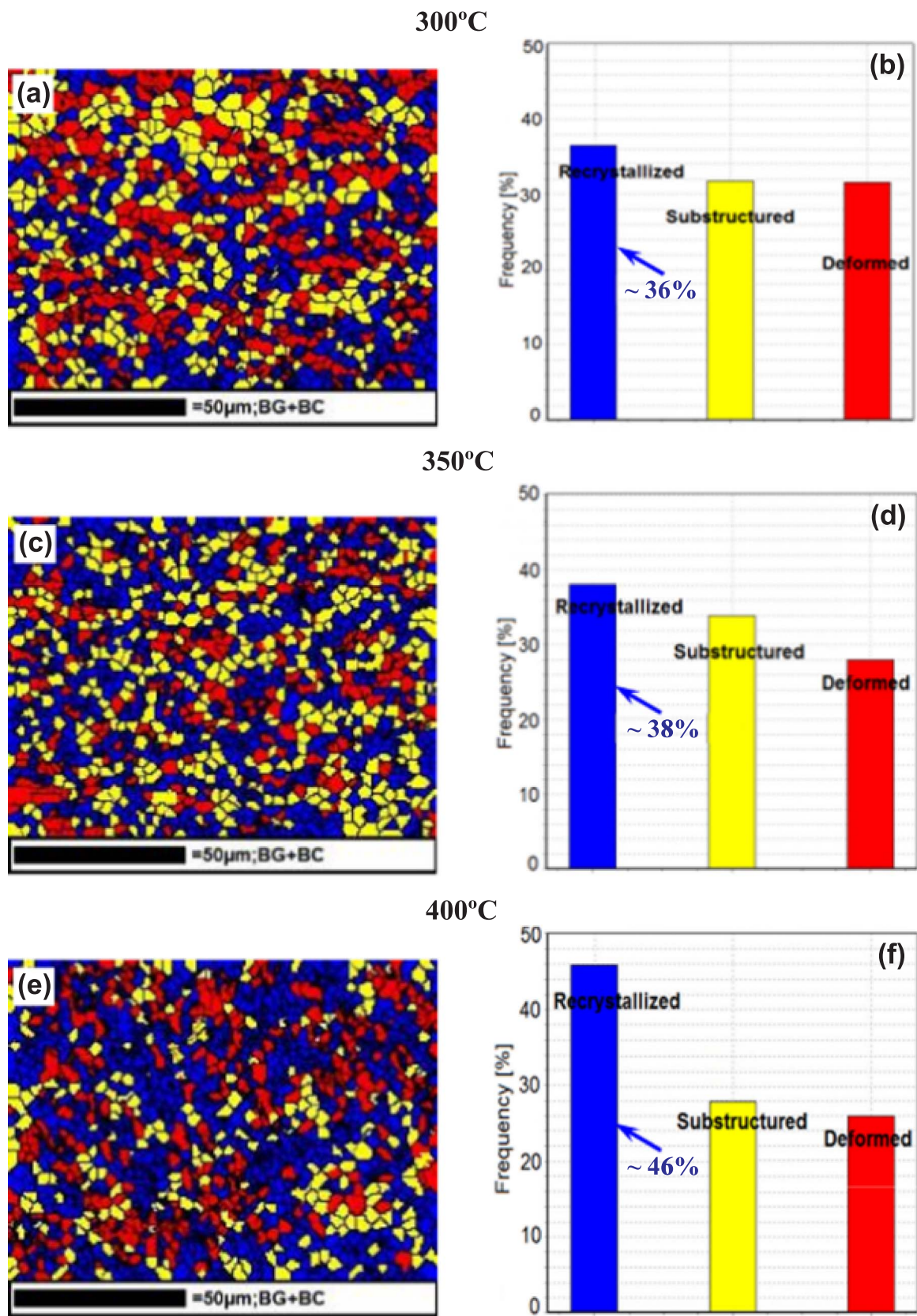


Fig. 10. EBSD recrystallized fraction component maps along with their quantification histograms of the 2024Al alloy deformed at (a, b) 300 °C, (c, d) 350 °C, and (e, f) 400 °C at a strain rate of 0.001 s^{-1} .

compression at 300 °C and 0.001 s^{-1} , a clear texture randomization and a split of intensity from P_1 (Fig. 11(a)) to P_2 and P_3 (Fig. 11(b)) were observed, with an intensity decrease to $\sim 3.0 \text{ MRD}$. At higher

temperatures (Fig. 11(c) and (d)), the splitting of intensities persisted with a decrease of MRD values from $\sim 2.9 \text{ MRD}$ at 350 °C (Fig. 11(c)), to $\sim 2.6 \text{ MRD}$ at 400 °C (Fig. 11(d)).

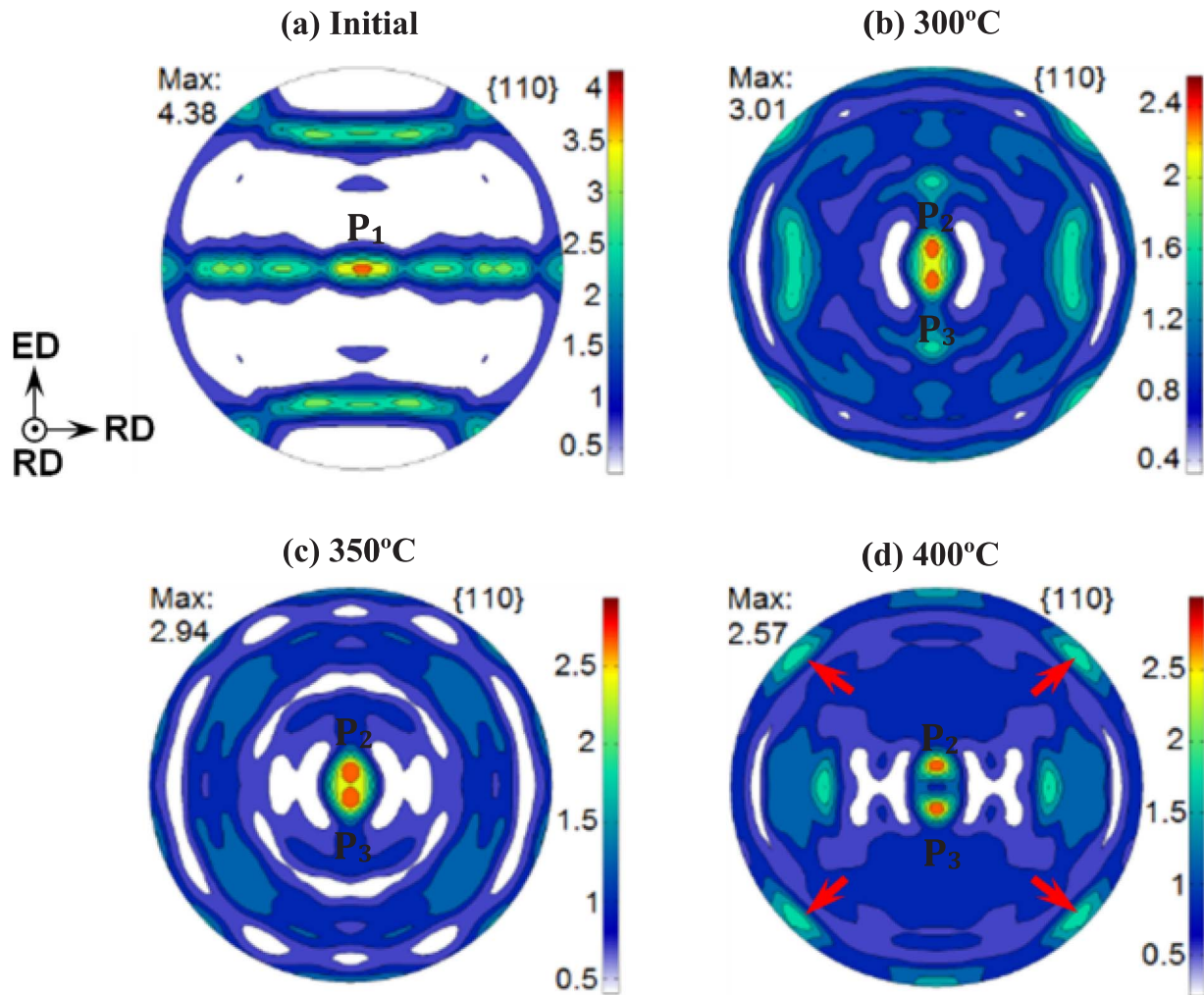


Fig. 11. $\{110\}$ pole figures of the 2.0 wt% CNT/2024Al nanocomposite (a) in the undeformed state, and after compression at (b) 300 °C, (c) 350 °C, and (d) 400 °C at a strain rate of 0.001 s^{-1} .

As described above, a maximum efficiency of power dissipation of $\sim 30\%$ was attained at 400 °C and 0.001 s^{-1} for the nanocomposite which corresponded to the condition of deformation of Fig. 11(d). The decreased intensity of P_2 and P_3 was likely related to the formation of new orientations, as indicated by the arrows in Fig. 11(d). “DRX texture component” could hence be identified for the nanocomposite through the two poles P_2 and P_3 . DRX was also observed in the high-temperature deformed microstructures of a composite fabricated with fine SiC_p and 2024Al powders [24], where the presence of fine SiC_p particles induced a high rate of dislocation generation in their vicinity during hot deformation, which represented preferred sites for the development of recrystallization nuclei [24]. It was also reported in [55] that the 2024Al with $8 \mu\text{m}$ SiC_p exhibited small equiaxed grains with a high dislocation density at temperatures of 320–400 °C, indicating that DRX occurred during hot deformation as well. The nucleation of DRX promoted by the presence of reinforcements leads to an increased dislocation density in the nearby matrix [47], which is consistent with the present 2.0 wt% CNT/2024Al nanocomposite. Furthermore, in the texture studies of deformed samples of AZ61+Sr alloy at 350 °C and 450 °C, it was reported that the texture became more random and the intensity of the components became lower with increasing deformation temperature [56]. Indeed, the increased fraction of recrystallized grains was always linked to texture weakening [57], and the volume fraction of recrystallized grains increased at higher temperatures and lower strain rates [11]. These results reported in the literature were in agreement with the observations in Fig. 11.

5. Conclusions

Via dynamic material modeling and Ziegler's instability criterion, 3D processing maps were constructed to reflect the continuous changes of power dissipation efficiency and flow instability domains in terms of temperature, strain rate, and strain. High-temperature compression tests for the 2024Al and the 2.0 wt% CNT/2024Al nanocomposite in a temperature range of 200–400 °C at a strain rate of 0.001 – 0.1 s^{-1} were conducted. The following conclusions could be drawn.

- 1) Single optimum domains of hot deformation for the alloy and nanocomposite were identified to be positioned at higher temperatures and lower strain rates, with a relatively smaller processing window for the nanocomposite due to the presence of CNTs and the more complicated microstructural features.
- 2) The processing maps revealed that the maximum efficiency of power dissipation obtained at 400 °C and 0.001 s^{-1} was $\sim 39\%$ for the 2024Al alloy and $\sim 30\%$ for the 2.0 wt% CNT/2024Al nanocomposite.
- 3) Instability was observed to occur at higher strain rates and lower temperatures for both alloy and nanocomposite. While the instable region at 0.01 s^{-1} almost vanished for the alloy, it still remained for the nanocomposite.
- 4) EBSD and XRD analyses revealed an increasing fraction of recrystallized grains with increasing deformation temperature, along with a more randomized texture accompanied by a decrease of

texture intensity. This corroborated the occurrence of dynamic recrystallization in the stable region of the alloy and nanocomposite.

Acknowledgements

The authors would like to thank the Natural Sciences and Engineering Research Council of Canada (NSERC) for providing financial support. This work was also financially supported by the National Key Research and Development Plan (No. 2017YFB0703100) and National Basic Research Program of China (No. 2011CB932603) and the CAS/SAFEA International Partnership Program for Creative Research Teams led by Professor Huiming Cheng (Institute of Metal Research, Chinese Academy of Sciences). One of the authors (D.L. Chen) is also grateful for the financial support by the Premier's Research Excellence Award (PREA), NSERC-Discovery Accelerator Supplement (DAS) Award, Canada Foundation for Innovation (CFI), and Ryerson Research Chair (RRC) program. The authors would also like to thank Messrs. A. Machin, Q. Li, C. Ma, J. Amankrah and R. Churaman for easy access to the laboratory facilities of Ryerson University and their assistance in the experiments.

References

- R.H. Baughman, A.A. Zakhidov, W.A. De Heer, Carbon nanotubes – the route toward applications, *Science* 297 (2002) 787–792.
- M.M. Shulaker, G. Hills, N. Patil, H. Wei, H.Y. Chen, H.S.P. Wong, et al., Carbon nanotube computer, *Nature* 501 (2013) 526–530.
- K.S. Munir, Y. Zheng, D. Zhang, J. Lin, Y. Li, C. Wen, Microstructure and mechanical properties of carbon nanotubes reinforced titanium matrix composites fabricated via spark plasma sintering, *Mater. Sci. Eng. A* 688 (2017) 505–523.
- P.C. Tsai, Y.R. Jeng, In-situ nanomechanical study on bending characteristics of individual multi-walled carbon nanotubes, *Mater. Sci. Eng. A* 658 (2016) 389–392.
- K.T. Lau, D. Hui, The revolutionary creation of new advanced materials-carbon nanotube composites, *Compos Part B* 33 (2002) 263–277.
- S. Zhao, Z. Zheng, Z. Huang, S. Dong, P. Luo, Z. Zhang, et al., Cu matrix composites reinforced with aligned carbon nanotubes: mechanical, electrical and thermal properties, *Mater. Sci. Eng. A* 675 (2016) 82–91.
- E.T. Thostenson, Z.F. Ren, T.W. Chou, Advances in the science and technology of carbon nanotubes and their composites: a review, *Compos Sci. Technol.* 61 (2001) 1899–1912.
- L. Zhang, Q. Wang, W. Liao, W. Guo, W. Li, H. Jiang, et al., Microstructure and mechanical properties of the carbon nanotubes reinforced AZ91D magnesium matrix composites processed by cyclic extrusion and compression, *Mater. Sci. Eng. A* 689 (2017) 427–434.
- P. Gao, M. Zhan, X. Fan, Z. Lei, Y. Cai, Hot deformation behavior and microstructure evolution of TA15 titanium alloy with nonuniform microstructure, *Mater. Sci. Eng. A* 689 (2017) 243–251.
- K. Wang, X. Li, Q. Li, G. Shu, G. Tang, Hot deformation behavior and microstructural evolution of particulate-reinforced AA6061/B₄C composite during compression at elevated temperature, *Mater. Sci. Eng. A* 696 (2017) 248–256.
- B. Li, Q.L. Pan, Z.M. Yin, Characterization of hot deformation behavior of as-homogenized Al-Cu-Li-Sc-Zr alloy using processing maps, *Mater. Sci. Eng. A* 614 (2014) 199–206.
- S. Samal, M.R. Rahul, R.S. Kottada, G. Phanikumar, Hot deformation behavior and processing map of Co-Cu-Fe-Ni-Ti eutectic high entropy alloy, *Mater. Sci. Eng. A* 664 (2016) 227–235.
- M. Sarebanzadeh, R. Mahmudi, R. Roumina, Constitutive analysis and processing map of an extruded Mg-3Gd-1Zn alloy under hot shear deformation, *Mater. Sci. Eng. A* 637 (2015) 155–161.
- N. Tahreen, D.F. Zhang, F.S. Pan, X.Q. Jiang, D.Y. Li, D.L. Chen, Hot deformation and processing map of an as-extruded Mg-Zn-Mn-Y alloy containing I and W phases, *Mater. Des.* 87 (2015) 245–255.
- J.Q. Li, J. Liu, Z.S. Cui, Characterization of hot deformation behavior of extruded ZK60 magnesium alloy using 3D processing maps, *Mater. Des.* 56 (2014) 889–897.
- C. Shi, X.G. Chen, Hot workability and processing maps of 7150 aluminum alloys with Zr and V additions, *J. Mater. Eng. Perform.* 24 (2015) 2126–2139.
- S. Wang, L.G. Hou, J.R. Luo, J.S. Zhang, L.Z. Zhuang, Characterization of hot workability in AA7050 aluminum alloy using activation energy and 3-D processing map, *J. Mater. Proc. Technol.* 225 (2015) 110–121.
- S. Gangolu, A. Gourav Rao, I. Sabirov, B.P. Kashyap, N. Prabhu, V.P. Deshmukh, Development of constitutive relationship and processing map for Al-6-65Si-0.44Mg alloy and its composite with B₄C particulates, *Mater. Sci. Eng. A* 655 (2016) 256–264.
- S.B. Bhimavarapu, A.K. Maheshwari, D. Bhargava, S.P. Narayan, Compressive deformation behavior of Al2024 alloy using 2D and 4D processing maps, *J. Mater. Sci.* 46 (3191) (2011) 9.
- L. Chen, G. Zhao, J. Gong, X. Chen, M. Chen, Hot deformation behaviors and processing maps of 2024 aluminum alloy in as-cast and homogenized state, *J. Mater. Eng. Perform.* 24 (2015) 5002–5012.
- Y. Zhang, Z. Chai, A.A. Volinsky, B. Tian, H. Sun, P. Liu, et al., Processing maps for the Cu-Cr-Zr-Y alloy hot deformation behavior, *Mater. Sci. Eng. A* 662 (2016) 320–329.
- D.X. Wen, Y.C. Lin, J. Chen, J. Deng, X.M. Chen, J.L. Zhang, et al., Effects of initial aging time on processing map and microstructures of a nickel-based superalloy, *Mater. Sci. Eng. A* 620 (2015) 319–332.
- H. Ahamed, V. Senthilkumar, Hot deformation behavior of mechanically alloyed Al6063/0.75Al₂O₃/0.75Y₂O₃ nano-composite-a study using constitutive modeling and processing map, *Mater. Sci. Eng. A* 539 (2012) 349–359.
- J.C. Shao, B.L. Xiao, Q.Z. Wang, Z.Y. Ma, Y. Liu, K. Yang, Constitutive flow behavior and hot workability of powder metallurgy processed 20 vol%SiCp/2024Al composite, *Mater. Sci. Eng. A* 527 (7865) (2010) 72.
- J. Liu, Z. Cui, C. Li, Analysis of metal workability by integration of FEM and 3-D processing maps, *J. Mater. Proc. Technol.* 205 (2008) 497–505.
- Y. Sun, L.X. Hu, J.S. Ren, Investigation on the hot deformation behavior of powder metallurgy Ti Al-based alloy using 3D processing map, *Mater. Charact.* 100 (2015) 163–169.
- S.K. Shaha, F. Czerwinski, W. Kasprzak, A. Friedman, D.L. Chen, Effect of Zr, V and Ti on hot compression behavior of the Al-Si cast alloy for powertrain applications, *J. Alloy. Compd.* 615 (2014) 1019–1031.
- J.C. Malas, S. Venugopal, Seshacharyulu, Effect of microstructural complexity on the hot deformation behavior of aluminum alloy 2024, *Mater. Sci. Eng. A* 368 (2004) 41–47.
- F. Bachmann, F.R. Hielscher, H. Schaeben, Texture analysis with MTEX – free and open source software toolbox, *Solid State Phenom.* 160 (2010) 63–68.
- F. Mokdad, D.L. Chen, Z.Y. Liu, B.L. Xiao, D.R. Ni, Z.Y. Ma, Deformation and strengthening mechanisms of a carbon nanotube reinforced aluminum composite, *Carbon* 104 (2016) 64–77.
- F. Mokdad, D.L. Chen, Z.Y. Liu, B.L. Xiao, D.R. Ni, Z.Y. Ma, Hot deformation and activation energy of CNT-reinforced aluminum matrix nanocomposite, *Mater. Sci. Eng. A* 695 (2017) 322–331.
- R.P. Bustamante, F.P. Bustamante, W.A. Flores, J.M.H. Ramirez, Al2024-CNTs composites by mechanical alloying, *Microsc. Microanal.* 16 (2010) 1256–1257.
- L. Yan, Z. Tan, G. Ji, Z. Li, G. Fan, D. Schryvers, et al., A quantitative method to characterize the Al₄C₃-formed interfacial reaction: the case study of MWCNT/Al composites, *Mater. Charact.* 112 (2016) 213–218.
- G. Fan, R. Xu, Z. Tan, D. Zhang, Z. Li, Development of flake powder metallurgy in fabricating metal matrix composites: a review, *Acta Metall. Sin.* 27 (2014) 806–815.
- H. Wei, Z. Li, D.B. Xiong, Z. Tan, G. Fan, Z. Qin, et al., Towards strong and stiff carbon nanotube-reinforced high-strength aluminum alloy composites through a microlaminated architecture design, *Scr. Mater.* 75 (2014) 30–33.
- J. Liao, M.J. Tan, R.V. Ramanujan, S. Shukla, Carbon nanotube evolution in aluminum matrix during composite fabrication process, *Mater. Sci. Forum* 690 (2011) 294–297.
- B. Xiao, Z.Y. Ma, J. Bi, Investigation on superplasticity in SiC_p/2024 cold rolling sheet after heat treatment, *J. Mater. Sci. Technol.* 19 (2003) 382–384.
- S. Suarez, E.R. Moore, B. Lechthaler, F. Mucklich, Grain growth analysis of multi-walled carbon nanotube-reinforced bulk Ni composites, *Carbon* 70 (2014) 173–178.
- H.J. Choi, B.H. Min, J.H. Shin, D.H. Bae, Strengthening in nanostructured 2024 aluminum alloy and its composites containing carbon nanotubes, *Compos. Part A* 42 (2011) 1438–1444.
- F.J. Humphreys, M. Heatherly, Recrystallization and Related Annealing Phenomena, Pergamon Press, Oxford, 1995.
- W.J. Kim, Y.J. Yu, The effect of the addition of multiwalled carbon nanotubes on the uniform distribution of TiC nanoparticles in aluminum nanocomposites, *Scr. Mater.* 72 (2014) 25–28.
- H.J. Choi, J.H. Shin, D.H. Bae, Grain size effect on the strengthening behavior of aluminum-based composites containing multi-walled carbon nanotubes, *Compos Sci. Technol.* 71 (2011) 1699–1705.
- Q. Liu, L. Ke, F. Liu, C. Huang, L. Xing, Microstructure and mechanical property of multi-walled carbon nanotubes reinforced aluminum matrix composites fabricated by friction stir processing, *Mater. Des.* 45 (2013) 343–348.
- H. Zare, M. Jahedi, M.R. Toroghinejad, M. Meratian, M. Knezevic, Microstructures and mechanical properties of carbon nanotubes reinforced aluminum matrix composites synthesized via equal-channel angular pressing, *Mater. Sci. Eng. A* 670 (2016) 205–216.
- A.A. Khamei, K. Dehghani, R. Mahmudi, Modeling the hot ductility of AA6061 aluminum alloy after severe plastic deformation, *JOM* 67 (2015) 966–972.
- J.R. Davis, Aluminum and Aluminum Alloys, ASM International, Materials Park, Ohio, USA, 1993.
- F.A. Mirza, D.L. Chen, A unified model for the prediction of yield strength in particulate-reinforced metal matrix nanocomposites, *Materials* 8 (2015) 5138–5153.
- J.G. Park, D.H. Keum, Y.H. Lee, Strengthening mechanisms in carbon nanotube reinforced aluminum composites, *Carbon* 95 (2015) 690–698.
- J. Guo, S. Amira, P. Gougeon, X.G. Chen, Effect of the surface preparation techniques on the EBSD analysis of a friction stir welded AA1100-B₄C metal matrix composite, *Mater. Charact.* 62 (2011) 865–877.
- Y. Zhao, H.L. Suo, M. Liu, D. He, Y.X. Zhang, L. Ma, et al., Highly reinforced and cube textured Ni alloy composite substrates by a hybrid route, *Acta Mater.* 55 (2007) 2609–2614.
- R. Bauri, D. Yadav, C.N. Shyam Kumar, B. Balaji, Tungsten particle reinforced Al5083 composite with high strength and ductility, *Mater. Sci. Eng. A* 620 (2015) 67–75.
- F. Mokdad, D.L. Chen, Cyclic deformation and anelastic behavior of ZEK100 magnesium alloy: effect of strain ratio, *Mater. Sci. Eng. A* 640 (2015) 243–258.
- H. Mirzadeh, J.M. Cabrera, A. Najafzadeh, P.R. Calvillo, EBSD study of a hot

- deformed austenitic stainless steel, *Mater. Sci. Eng. A* 538 (2012) 236–245.
- [54] T. Sakai, A. Belyakov, R. Kaibyshev, H. Miura, J.J. Jonas, Dynamic and post-dynamic recrystallization under hot, cold, and severe plastic deformation conditions, *Prog. Mater. Sci.* 60 (2014) 130–207.
- [55] B.C. Ko, Y.C. Yoo, Prediction of dynamic recrystallization condition by deformation efficiency for Al2024 composite reinforced with SiC particle, *J. Mater. Sci.* 35 (2000) 4073–4077.
- [56] S.A. Sani, G.R. Ebrahimi, A.R. Kiani Rashid, Hot deformation behavior and dynamic recrystallization kinetics of AZ61 and AZ61 + Sr magnesium alloys, *J. Mag. Alloy.* 4 (2016) 104–114.
- [57] X. Xia, K. Zhang, X. Li, M. Ma, Y. Li, Microstructure and texture of coarse-grained Mg-Gd-Y-Nd-Zr alloy after hot compression, *Mater. Des.* 44 (2013) 521–527.